Solidification of Al Alloys under Electromagnetic Pulses and Characterization of 3D Microstructures using Synchrotron X-ray Tomography

T. Manuwong[1], W. Zhang[1], P.L.Kazinczi[1], A.J. Bodey[2], C. Rau[2], J. Mi[1*]

[1]School of Engineering, University of Hull, Hull, East Yorkshire, HU6 7RX, UK

[2]Diamond Light Source, Oxfordshire, OX11 0DE, UK

Keywords: Synchrotron X-ray, Tomography, Electro-magnetic Pulse, Solidification, Al alloys.

*Corresponding authors: J. Mi, email: j.mi@hull.ac.uk

ABSTRACT

A novel programmable electro-magnetic pulse device was developed and used to study the solidification of Al-15%Cu and Al-35%Cu alloys. The pulsed magnetic fluxes and Lorentz forces generated inside the solidifying melts were simulated using finite element methods, and their effects on the solidification microstructures were characterized using electron microscopy and synchrotron X-ray tomography. Using a discharging voltage of 120V, a pulsed magnetic field with the peak Lorentz force of ~1.6 N was generated inside the solidifying Al-Cu melts which was showed sufficiently enough to disrupt the growth of the primary Al dendrites and the Al_2Cu intermetallic phases. The microstructures exhibit a strong correlation to the characteristics of the applied pulse, forming a periodical pattern that resonate the frequency of the applied electro-magnetic field.

I. INTRODUCTION

Almost all metallic alloys are manufactured via the solidification processes, and the mechanical properties of the cast ingots or components, such as the strength, ductility, fatigue life, etc, are, predominantly determined by the as-cast grain microstructure formed during the solidification processes [1, 2]. The as-cast grain microstructures also affect, to a certain degree, the grain structures formed during any subsequent thermomechanical deformation and/or heat-treatment processes [1, 3]. In general, uniformly-distributed polygonal grains are desirable for higher strength as revealed by the classical Hall-Petch relationship [4], i.e. the yield strength (σ_y) increases linearly with the inverse of square-root of the grain size ($\frac{1}{\sqrt{d}}$) of the materials ($\sigma_y \sim \frac{1}{\sqrt{d}}$). In industry, the most common practice to control the solidification microstructure is to add external grain refiners during the solidification processes. The typical examples are Al-Ti-B for Al alloys [5, 6], Zr for Mg-based alloys [7], B for Ti-based alloys [8] and Ce for steel [9]. However, there are no universal grain refiners that are suitable for all metallic alloys, and adding grain refiners often result in extra cost, and sometimes contamination to the alloy chemistry. As the environmental impact and sustainable development become important issues in all industry [10], the metallurgical and metal manufacturing industry have been seeking to develop more

environmental friendly technologies for grain refinement without or much less of adding external grain refiners during the solidification processes [11]. In the past 30 years or so, many physical field based methods have been investigated with the aim to develop a generic method for grain refinement that is suitable for all metallic alloys regardless of the chemistry. For example, applying ultrasonic wave [12] or electrical current, or magnetic field into the solidifying alloy melts to enhance grain nucleation and control grain growth [13-16]. Technically, the external fields or energy can be applied into the melts via probes that have direct contact with the melts, such as sonotrodes for ultrasonic wave, or electrodes for electrical current; or through a non-contact manner such as electromagnetic inductive coupling [17]. For the direct contact methods, special materials are often needed for making the sonotrodes or electrodes to withstand the erosion of high-temperature melts. So far no robust solutions have been found to sustain high melting point alloys, e.g. Ni-based alloys, steels, etc. The electromagnetic inductive coupling methods have the advantages of non-contact, but often need high electrical current or voltage inputs to generate enough Lorenz forces or convective flows inside the melts in order to change the growth of solidification microstructure [18, 19]. The high energy inputs often result in inductive heating of the melts, which is, in general, a negative effect for controlling grain growth, and unwanted consumption of energy [20].

Recently, a number of pulsed magnetic field methods, such as pulsed magneto oscillation (PMO) [21] have been developed and showed the effectiveness in refining solidification microstructure of Al [22], Mg [19], Cu [23], Ti [24] alloys and Steels [25] with relatively low consumption of energy. However, most of the laboratory based research so far has applied the electro-magnetic pulses into a melt held in a stationary crucible [26, 27]. There have been very limited reports on applying this method in a semi-continuous or continuous casting operation [24]. Furthermore, for all previous studies in this field, microstructural analyses on the samples cast under the pulsed electro-magnetic fields were made in two dimension using optical or electron microscopes. The three dimensional (3D) characteristics of the microstructures solidified under pulsed electro-magnetic field have not been seen reported.

In this research, we designed a novel programmable electro-magnetic pulse (EMP) device and a small scale solidification apparatus to mimic the semi-continuous direct chill (DC) casting process. Electro-magnetic pulses with the discharging voltages of 120 V and a frequency of 1 Hz were applied to Al-15%Cu and Al-35%Cu alloy samples during the solidification with accurately controlled thermal gradients and withdrawal speeds out of the furnace (40 μm/s for Al-15%Cu and 30 μm/s for Al-35%Cu). Synchrotron X-ray tomography technique was used to characterise the primary Al_2Cu phases and the Al dendrites, and the effects of the pulse parameters on the resulting 3D microstructure were quantified for the first time.

II THE EXPERIMENTAL APPARATUS

A *The programmable electro-magnetic pulse device*

A programmable EMP device was designed, built and commissioned for this research. It consists of two main units: the energy charging unit and pulse generating unit, and the conceptual circuit design is showed in Fig. 1. In the energy charging unit, A variable transformer (Carroll & Meynell, 6.72 kVA Variac, 240V AC, 28A) was used to firstly transform the standard 240 V AC current delivered from the mains of the laboratory into currents of variable voltages (10 ~ 270 V) and then to charge the capacitor bank (2050μF 800V), which was made by connecting in parallel two series of capacitor banks (five capacitors in each series with each

having the properties of 820μF 400V). The voltage charged into the capacitor and the time needed for the charging; and the energy (E) stored inside the capacitor bank can be calculated by [28, 29]:

$$V_c = V\left(1 - e^{\left(\frac{-t}{R_1 C}\right)}\right), t = -R_1 C \ln(1 - \frac{V_c}{V}) \quad (1)$$

$$E = 0.5\mathrm{C}\, V_c^{\,2} \quad (2)$$

Where V is the charging voltage delivered from the transformer, V_c is the voltage charged into the capacitor bank, t is time, R_1 is the resistor that was placed into the charging unit to regulate the current through the charging circuit in order to control the charging time (R_1 = 22 Ω in this case), C is a capacitance of capacitor bank. E is the energy stored inside the capacitor bank. Fig. 1 also shows a typical profile of the voltage charged into the capacitor bank using a 120 V current from the transformer, and the capacitor bank was fully charged in ~ 225.5 ms.

In the pulse generating unit, the energy stored in the capacitor bank can be discharged into the working unit, i.e. a helix copper coil in this case (Fig. 1) in a controlled short period of time to generate short but high peak current [26] or magnetic flux pulse. The voltage discharged and the time needed to fully discharge can be calculated by:

$$V_d = V_c e^{\left(\frac{-t}{R_2 C}\right)}, t = -R_2 C \ln(\frac{V_d}{V_c}) \quad (3)$$

Where V_d is the voltage discharged from the capacitor bank, R_2 = 0.049 Ω is the resistance of the copper coil.

The novelty of this device is that a Thyrister trigger switch was designed and integrated into the discharging circuit to control and regulate the release of the energy stored inside the capacitor bank in term of time, duration and repetition. In this way, programmable high magnetic flux pulses with tuneable amplitudes, frequencies and duration can be generated to suit different alloys systems for process optimisation purpose. The maximum charging and discharging voltage for this EMP device is ~ 270 V, limited by the capacity of the Variac transformer. Based on Eq. (1) and (3), the capacitor bank can be fully charged in 5 × R_1C = 225.5 ms (where R_1C = 22 Ω × 0.002050 F) while the energy discharges from the capacitor bank to the coil normally take 5 × R_2C = ~ 0.501 ms (R_2 C= 0.049 Ω × 0.002050F), respectively. Therefore, the frequency of EMP device can be tuned in the range of 1 - 5 Hz.

Fig. 1 also shows that, using this trigger unit, the 120 V electrical energy stored in the capacity bank can be converted to a current pulse with the peak current calculated at ~ 2449 A.

B *The solidification apparatus*

A small-scale solidification apparatus was designed and built as schematically showed in Fig. 2. It consists of (1) a furnace made by Ni-Cr heating wire (22 SWG and 15 meters long) held in a tube-shaped chamber made by mouldable mastics, and a PID close-loop temperature control unit (Omega, model CN8201), (2) a sample stage to hold quartz tubes (as the crucible) to contain liquid metal, and (3) a precision linear stage (model T-LSR075A made by Zaber Technologies Inc.). It has the maximum travel distance of 75 mm with a step resolution of 0.49 μm/s, allowing a very accurate control of the withdrawal of the quartz tubes out of the furnace, and mimicking the semi-continuous DC casting operation.

The helix coil (40 mm inner diameter and 120 mm long) for generating the magnetic pulse was wound by using Ø2 mm enamelled copper wire.

III. THE PULSED MAGNETIC FLUXES

A *The measured magnetic flux pulses*

The magnetic flux pulses generated inside the quartz tube (without the liquid metal present) by different voltages (40, 80, 120, 160 V) discharged from the capacitor bank were measured using a Gaussmeter (Hirst Gauss Meter, model GM08) at the location P1 showed in Fig. 3a and plotted in Fig. 3b.

The measured magnetic flux pulses exhibited the similar shape with the peak values of approximately 300, 570, 900 and 1100 mT for the 40, 80, 120 and 160V discharging voltages, respectively. The corresponding full width at half maximum (FWHM) for each case was measured at 0.25, 0.45, 0.55 and 0.65 ms (Fig. 3c), respectively. Clearly, all magnetic pulses generated by different discharging voltage occurred in < 1ms.

B *The simulated magnetic flux pulses*

To obtain the information concerning the magnetic flux pulses generated inside the liquid metal, finite element simulation was carried out using a commercial software, COMSOL Multiphysics v5.0. The geometry model consists of the domains for (1) the liquid metal alloys, (2) the quartz tube, (3) the helix coil (45 turns), and (4) the space occupied by air. Fig. 2b and 2c show the middle part of the 2D axis-symmetry geometry model and the finite element mesh used in the simulation (triangular meshes of 94,262 elements).

The helix coil was defined as the Single-Turn Coil domain and each turn of the coil was assumed to be evenly symmetrical [30]. The magnetic flux density of this coil was calculated using the equations below [31].

$$0 = \nabla \cdot \boldsymbol{B} \tag{4}$$

$$\nabla \times \mathbf{B} = C\,\mu_0 \mu_r \boldsymbol{J_e} \tag{5}$$

$$\boldsymbol{J_e} = \frac{\mathrm{V}_d}{\mathrm{A}\,R_2} \tag{6}$$

where $\boldsymbol{B}$ is the magnitude of the magnetic field (the magnetic flux density measured by Tesla (T)), μ_o is the permeability of free space (1.26×10^{-6} T m/A), μ_r is the relative permeability of copper, $\boldsymbol{J_e}$ is current density passing through the coil, V_d is the discharging voltage, R_2 is the electrical resistance of the coil, A is area cross-section of coil wire, and C is the compensation coefficient of the coil because of joule heat (in this experiment C is assumed 0.85) [32].

The key materials properties used in the simulation are listed in Table I.

Table I. The materials properties used in the simulation [33-39]

	Al-35%Cu	Al-15%Cu	Air	Copper coil	Quartz tube
Density (g/cm^3)	4.76	3.63	1.2×10^{-3}	8.7	2.2
Relative Permeability	1.11	1.11	1	1	1
Resistivity (Ω m)	15.82×10^{-8}	11.85×10^{-8}	2.3×10^{16}	1.6×10^{-8}	1×10^{6}
Viscosity (mPa S)	2.1	2.48	0.037	-	-

Fig. 3 shows the measured and the simulated magnetic flux densities generated by different discharging voltages, and they all exhibited the similar profiles. The peak values of the simulated pulses with C = 1 in Eq. (5) are 15% higher than those of the measured pulses for each discharging voltage. These are mainly because, in the modelling, the energy losses in the discharging circuit and the coil, such as the generation of heat, were not considered. Fig. 3c shows that if C = 0.85 is assumed and used in Eq. (5). The simulated peak values almost match those of the measured peak values, and the differences of peak values between the measured and the simulated magnetic flux densities for all the discharging voltages are within 2%. This indicates that the designed EMP device has an energy conversion efficiency of 85%, i.e. 85% of the stored energy can be transferred as the pulsed energy into the liquid metal.

Furthermore, it is noteworthy to find that the peak values of the magnetic flux density pulses increase proportionally to the discharging voltages as showed in Fig. 3d with a slope of 6.9 mT/V.

C *The pulsed Lorentz force*

Through the helix coil, induced current is generated inside the liquid alloy and it can be calculated by [31]

$$\boldsymbol{J} = \nabla \times (\mu_0^{-1}\mu_r{}^{-1}\boldsymbol{B}) \tag{7}$$

Where $\boldsymbol{J}$ is the induced current flux inside the molten alloy, and $\boldsymbol{B}$ is induced magnetic flux density.

Fig. 3e illustrates the induced current fluxes generated with respect to the different discharging voltages at the measurement point P2. The induced current flux increases as the discharging voltage increases.

The pulsed Lorentz forces ($\boldsymbol{F}$) that are generated inside the liquid alloy contained inside the quartz tube can be calculated by [20, 21]:

$$\boldsymbol{F} = \boldsymbol{J} \times \boldsymbol{B} \tag{8}$$

Fig. 3f shows the Lorentz forces generated by the induced current with the different discharging voltages (40, 80, 120 and 160V), which were simulated again using Comsol Multiphysics v5.0 with the same computational domain and mesh structure. The Lorentz forces

act on the liquid metal and point towards the symmetric axis of the quartz tube. The simulation shows that, as the discharging voltages increased from 40 to 160 V, the Lorentz force at the measurement point, P2, increased from 0.16 to 2.7 N.

IV. SOLIDIFICATION EXPERIMENT

Al-15%Cu and Al-35%Cu alloys were used, and they were made by melting together pure Al (purity of 99.97%), and pure Cu (purity of 99.97%) with the correct weight ratio in a Carbolite furnace. The alloys were casted into 130 mm long quartz tube with an inner diameter of 9 mm by using a small custom-made counter-gravity casting apparatus. The controlled negative pressure drew the liquid metal uphill to fill into the glass tubes in a quiescent manner, avoiding the surface turbulence of the liquid metal during the filling process and therefore any entrainment of air bubbles or oxide films during filling were minimized.

Quartz tubes were again used (130 mm long with 9 mm inner diameter) as the casting moulds. The alloy ingots were placed into the quartz tubes, and at the bottom end, the quartz tubes were sealed by Duratec ceramic rods which were placed and linked to a linear stage with a programmable travel speed range of 0.49 ~ 100 μm/s. Three K-type thermocouples were positioned inside the glass tubes at 10, 50 and 90 mm from the bottom of the sample to measure the temperature at those locations during the experiment, and the temperature was recorded using a data logger (TC-08), and PicoLog for Windows (PLW) software.

The quartz tube with alloy rod inside was heated in the furnace showed in Fig. 2a and hold above the alloy melting point for 1 hour to homogenise the melt temperature. Then the quartz tubes with the melt were withdrawn out of the furnace at a constant speed of 40 μm/s for the Al-15%Cu sample, and 30 μm/s for the Al-35%Cu sample, respectively.

Two groups of samples were casted, one with and the other without EMP. For the case with EMP, the discharge voltage of 120V with a frequency of 1 Hz was applied continuously for each sample, after the quartz tubes were withdrawn out of the furnace, until the alloy was completely solidified.

After solidification, the as-cast alloy samples were taken out of the quartz tubes, and were sectioned longitudinally into two halves. The sectioned surfaces were ground using SiC grinding papers of 600, 1200, 2500 grid, then polished using diamond suspension of 6 and 1 μm and colloidal silica suspension using Motopol 12 grinder and polisher operated at 150 rpm. Each grinding and polishing step took 20~30 minutes.

V. SYNCHROTRON X-RAY TOMOGRAPHY ANALYSIS

Synchrotron X-ray tomography measurements of the 3D microstructures of the solidified samples were carried out at Beamline I13-2 of Diamond Light Source, UK. Needle-shaped samples (~1 mm in diameter and ~20 mm in height) were mounted on the sample stage as shown in Fig. 4. A polychromatic beam (8-30 keV) of parallel geometry was used, with the lower energies (< 8 KeV) suppressed by filters (2 mm Al, 10 μm Cu and 30 μm Pd). 4001 projection images (17.5 ms exposure time for each projection) were collected at a fixed angle step over 180° via flyscanning. Images were collected by a $CdWO_4$ scintillator-coupled pco.edge 5.5 (PCO AG, Germany) detector. Visual light optics within the detector assembly provided 8× magnification, giving an effective pixel size of 0.81 μm and a field of view of 2.1 × 1.8mm. The distance between sample and scintillator was set at 20 mm, chosen to give low levels of in-line

phase contrast. Data were reconstructed with the tomographic reconstruction module of DAWN v1.7 [40, 41]. Projection images were flat and dark corrected, and then reconstructed using a filtered back projection [42] algorithm which incorporated ring artefact suppression (ParameterR = 0.005, NumSeries = 1) [43]. Threshold-based segmentation was performed in Avizo v8.0 (FEI, USA). The reconstruction procedure is briefly illustrated in Fig. 4.

VI. RESULTS AND DISSCUSSION

A The effect of EMP on the grain growth and dendrite morphology

Fig. 5 shows the 2D and 3D microstructures of the Al-15%Cu and Al-35%Cu alloy, the micrographs showed in the left-hand column are the typical scanning electron microscopy images, the middle ones are the reconstructed 3D tomography data-set chosen from the typical area marked by the rectangular boxes on the SEM micrographs. While the right-hand 3D dataset are the segmented primary Al dendrites and the Al_2Cu phases extracted from the 3D dataset showed in the middle column.

When cast without EMP, the primary Al dendrites of Al-15%Cu grew unidirectionally against the direction of withdrawal of the quartz tube and formed large and long columnar dendrites as seen in Fig. 5a-1, a-2 with the size of approximately 200-400 μm long. Similarly, without EMP, the primary intermetallic phases (Al_2Cu) of Al-35%Cu also grew into long phases (Fig. 5c-1) with the size of approximately ~50 μm wide and 700 ~1,000 μm long.

When EMP applied, it can be clearly seen that the long columnar dendritic microstructure of the Al-15%Cu was disrupted (Fig. 5b-1, b-2), forming smaller and randomly oriented dendrites with the average size of approximately 50-100 μm (Fig. 5b-2, b-3). While, for the Al-35%Cu alloy, most long primary Al_2Cu phases were shortened to approximately ~100 μm long, and the growth direction of some Al_2Cu phases changed, no longer perfectly aligned in parallel with the withdrawal direction of the quartz mould as in the case of without EMP.

However, for both alloys cast without and with EMP, the eutectic phases remained the similar morphology.

The 3D tomography datasets showed in the middle column provide convincing experimental evidences that the pulsed Lorentz forces generated inside the melt are strong enough to disrupt the growth of the primary Al dendrites in the Al-15%Cu alloy, and the primary Al_2Cu intermetallic phases in the Al-35%Cu alloy. The peak Lorentz force for the 120 V discharging voltage was calculated to be ~1.6 N, which is sufficient to move the liquid in front of the growing dendrites or primary phases to cause the changes of direction of growth and therefore to form the more randomly oriented dendrites (Fig. 5b-1, b-2), and the disrupted primary Al_2Cu phases (Fig. 5d-1, d-2).

It is more interesting to see that the majority of the primary Al_2Cu phases showed in Fig. 5d-1 exhibited the intermittent but periodic pattern because of the applied EMP, and at least 10 of the disrupted Al_2Cu primary phases showed in Fig. 5d-1 were measured at ~38 μm long. Some of the disrupted Al_2Cu primary phases were also captured in the 3D dataset (Fig. 5d-2). While the withdrawal speed of the quartz tube for the Al-35%Cu was 30 μm/s, and these evidences indicated that the growth of the primary Al_2Cu were more likely disrupted and even broken when the pulsed Lorentz forces come around in every second, despite not all Al_2Cu phases exhibited such as periodical patterns that resonate the frequency of the EMP applied. These may be due to

either the applied force were still not strong enough to cause a complete disruption to the growth of all primary Al_2Cu phases, or there were not enough free space for the growing Al_2Cu phases to move away from their original direction of growth, and then finally be "seen" after solidified. Hence detailed in-situ studies in the future are necessary to elucidate the phenomenon.

VII. CONCLUSION

A novel programmable electro-magnetic pulse device was designed and built for the studies of the effects of pulsed magnetic fields on the growth of primary dendrites and primary intermetallic phase in Al-Cu alloys. Using this device and a discharging voltage of 120V, a pulsed magnetic field with the peak Lorentz force of ~1.6 N can be generated inside the Al-Cu alloy melts, and it is sufficient enough to disrupt the growth of the primary Al dendrites and the Al_2Cu intermetallic phases. 2D and 3D synchrotron X-ray tomography characterisations reveal that the microstructures exhibit a strong correlation to the characteristics of the applied pulses, forming a periodical pattern that reflects precisely the frequency of the electromagnetic pulses.

ACKNOWLEDGEMENT

We would like to acknowledge Diamond Light Source for the award of synchrotron X-ray beam time on Beamline I13-2 under the proposal No. MT9974. The financial supports for this research from the Royal Thai Government PhD Studentship (for T. Manuwong), the joint University of Hull and Chinese Scholarship Council (UoH-CSC) PhD studentship (for W. Zhang) and the Royal Society Industry Fellowship (for J. Mi) are also gratefully acknowledged.

REFERENCES

[1] M.C. Flemings, solidification processing, MeGraw-Hill New York, 1974.
[2] J.A.Dantzig, M.Rappaz, Solidification, 1st ed., Taylor and Francis Group.LLC, 2009.
[3] J.A. Wert, N.E. Paton, C.H. Hamilton, M.W. Mahoney, Metallurgical and Materials Transactions A, 12A (1981) 1267-1176.
[4] E.O. Hall, Proceedings of the Physical Society Section B, 64 (1951).
[5] M. Johnsson, L. Backerud, G.K. Sigworth, Metallurgical Transactions A 24 (1993) 481-491
[6] G.P. Jones, J. Pearson, Metallurgical Transactions B 7(1976) 223-234
[7] C. Song, Q. Han, Q. Zhai, China foundry, 6 (2009) 93-103.
[8] S. Tamirisakandala, R.B. Bhat, J.S. Tiley, D.B. Miracle, Scripta Materialia, 53 (2005) 1421-1426.
[9] M. Guo, H. Suito, ISIJ International. , 39 (1999) 722-729.
[10] P. Koltun, Progress in Natural Science: Materials International, 20 (2010) 16-29.
[11] M. Garnier, ISIJ International, 30 (1990) 1-7.
[12] G.I. Eskin, D.G. Eskin, Ultrasonic Grain Refinement, Ultrasonic Treatment of Light Alloy Melts, Second Edition, CRC Press, 2014, pp. 129-170.
[13] L. Li, J.H. Ma, C.J. Song, Z.J. Li, Y.L. Gao, Q. Zhai, Journal of Iron and Steel Research, International, 16 (2009) 7-12.
[14] S. Eckert, P.A. Nikrityuk, D. RaBiger, K. Eckert, G. Gerbeth, Metallurgical and Materials Transactions B 38B (2007) 977-988.
[15] Y. Du, Y. Lu, T. Wang, T. Li, G. Zhang, Procedia Engineering 27 (2012) 1129 - 1134.
[16] S.H. Hanhn, Y. Sakai, T. Tsukada, M. Hozawa, N. Imaishi, S. Kitagawa, Metallurgical and Materials Transcations B, 29B (1998) 223-228.
[17] S. Asai, Science and Technology of Advanced Materials, 1 (2000) 191-200.

[18] T. Campanella, C. Charbon, M. Rappaz, Metallugical and Materials Transaction A 35A (2004) 3201-3210.
[19] M.J. Li, T. Tamura, N. Omura, K. Miwa, Transactions of Nonferrous Metals Society of China 20 (2010) 1192−1198
[20] Q. Li, C. Song, H. Li, Q. Zhai, Materials Science and Engineering A 466 (2007) 101-105.
[21] Z.X. Yin, Y.Y. Gong, B. Li, Y.F. Cheng, D. Liang, Q. Zhai, Journal of Materials Processing Technology, 212 (2012) 2629-2634.
[22] X. Li, Y. Fautrelle, K. Zaidat, A. Gagnoud, Z. Ren, R. Moreau, Y. Zhang, C. Esling, Journal of Crystal Growth, 312 (2010) 267-272.
[23] W. Dai, X. Wang, Materials Transactions, 51 (2010) 892-895.
[24] R. Chen, J. Yang, H. Ding, F. Huang, Y. Su, J. Guo, H. Fu, Journal of Materials Processing Technology, 212 (2012) 1934-1940.
[25] Z. Shu-cai, L. Hua-ji, R. Jin-song, R. Zheng-de, Z. Jie-xin, Y. Zhi-li, China foundry, 4 (2007) 198-201.
[26] Y.J. Zhang, G.J. Chen, C.L. Tang, J. Shanghai Jiaotong Univ. (Sci.), 17 (2012) 282-285.
[27] N. Pei, Y.Y. Gong, R. Li, Z. Xia, Q. Zhai, China foundry, 8 (2011) 47-50.
[28] E.G. Bakhoum, Journal of Renewable and Sustainable Energy, 4 (2012).
[29] S. Dan, L. Ning, Journal of Power and Energy Engineering, 2 (2014) 579-585.
[30] I. Quintana, Z. Azpilgain, D. Pardo, I. Hurtado, The COMSOL Conference Stuttgart, 2011
[31] E. Basham, Z. Yang, W. Liu, IEEE Transaction on Biomedical Circuits and Systems 54 (2008) 1-12.
[32] S. Bartkevičius, J. Novickij, Measurement Science Review, 7 (2007).
[33] D. Bernard, Ø. Nielsen, L. Salvoc, P. Cloetens, Materials Science and Engineering: A, 392 (2005) 112-120.
[34] C.Y. Ho, M.W. Ackerman, K.Y.Wu, T.N.Havill, R.H.Bogaard, R.A.Matula, S.G.Oh, H.M.James, J.Phys.Chem.Ref.Data, 12 (1983).
[35] Y. Plevachuk, V. Sklyarchuk, A. Yakymovych, S. Eckert, B. Willers, K. Eigenfeld, Metallugical and Materials Transaction A, 39A (2008).
[36] N.Y. Konstantinova, P.S. Popel, D.A. Yagodin, High temperature, 47 (2009).
[37] R.S. company, Fused quartz glass properties.
[38] S.D. Pawar, P. Murugavel, D.M. Lal, Journal of Geophysical Research: Atmospheres, 114 (2009) D02205.
[39] P. Guerrier, J.H. Hattel, International Conference on Advanced Manufacturing Engineering and Technologies 2013.
[40] A. Ashton, J. Aishima, M. Basham, P. Chang, B. El Kassaby, J. Filik, M. Gerring, K. Levik, I. Sikharulidze, M. Webber, (2014) ZENODO. zenodo.14084.
[41] M. Basham, J. Filik, M. T.Wharmby, P.C. Y.Chang, B.E. Kassaby, M. Gerring, A. W.Ashton, Journal of synchrotron radiation in publication (2015).
[42] G.N. Ramachandran, A.V. Lakshminarayanan, Proceedings of the National Academy of Sciences of the United States of America, 68 (1971) 2236-2240.
[43] S. Titarenko, P.J. Withers, A. Yagola, Applied Mathematics Letters, 23 (2010) 1489-1495.

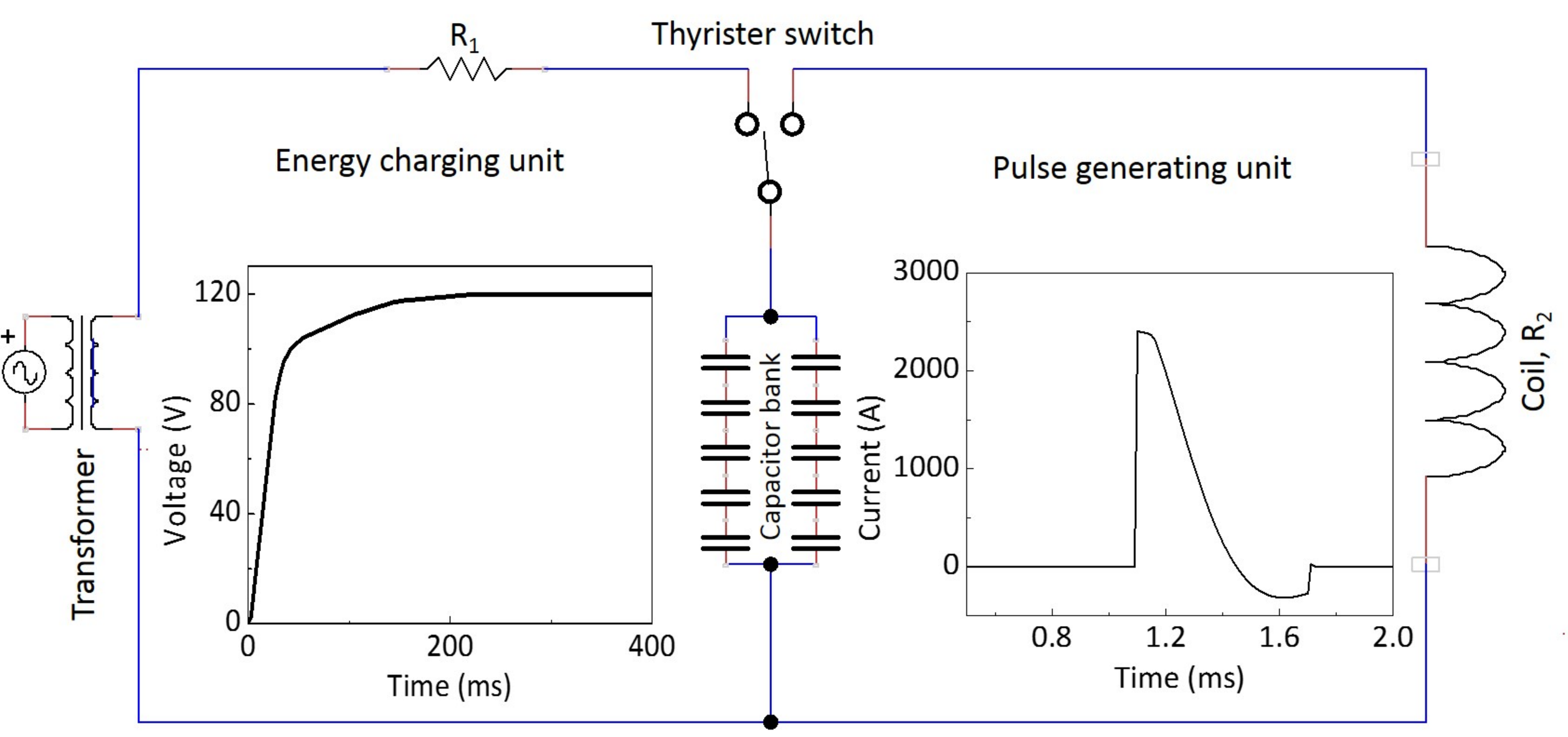

Fig. 1. A conceptual circuit design for the EMP device, including an energy charging unit and a pulse generating unit. Typical examples are also shown for the voltage charged into the capacitor bank and the pulsed current generated into the coil.

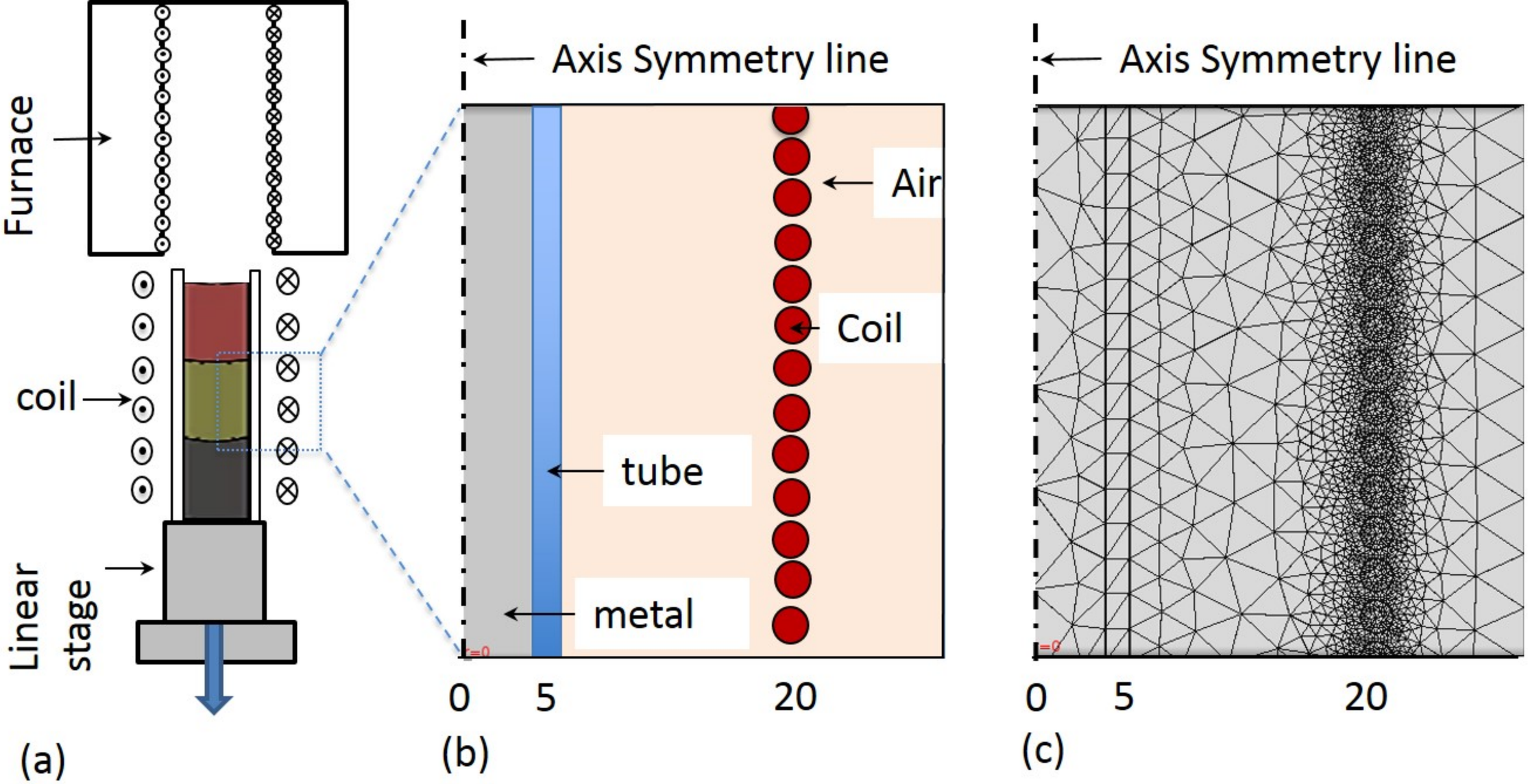

Fig. 2. (a) A schematic, showing the solidification apparatus, and (b) the middle part of the computational domain for the liquid metal, the quartz tube, the helix coil and the space occupied by air in the finite element simulation, and (c) the mesh structure used in the simulation.

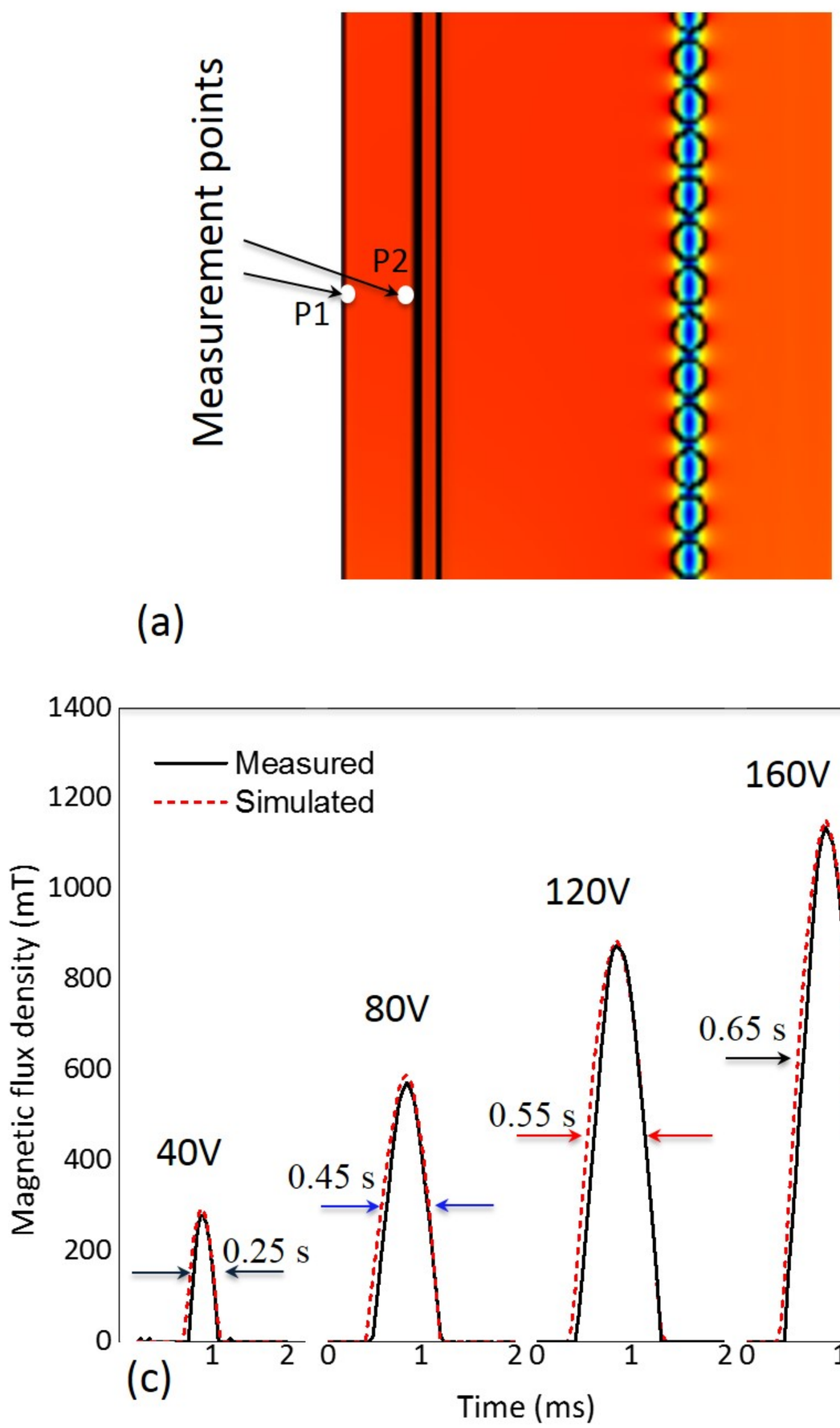

Fig. 3. (a) The locations where the magnetic flux density (P1), induced current and Lorentz force (P2) were measured, (b) comparison of the measured and simulated (C = 1) pulses of magnetic flux densities, and (c) those with C = 0.85; (d) the peaks of the magnetic flux density as the function of the discharging voltages, (e) the simulated induced current fluxes inside metal alloy, and (f) the simulated Lorentz forces.

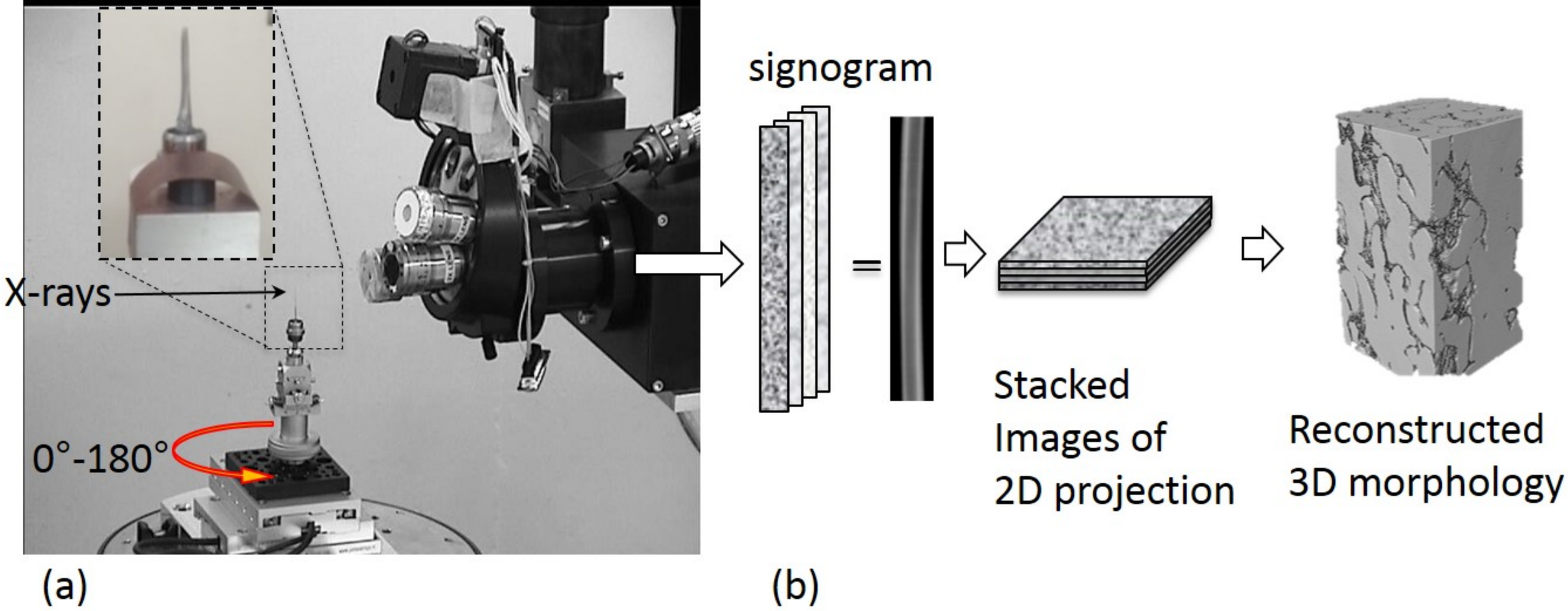

Fig. 4. (a) A photograph, showing a needle-shaped sample mounted on the sample stage, and the detector assembly at Beamline I13-2 of Diamond Light Source; (b) the illustrative procedure for the acquisition and reconstruction of the 3D tomography data-set.

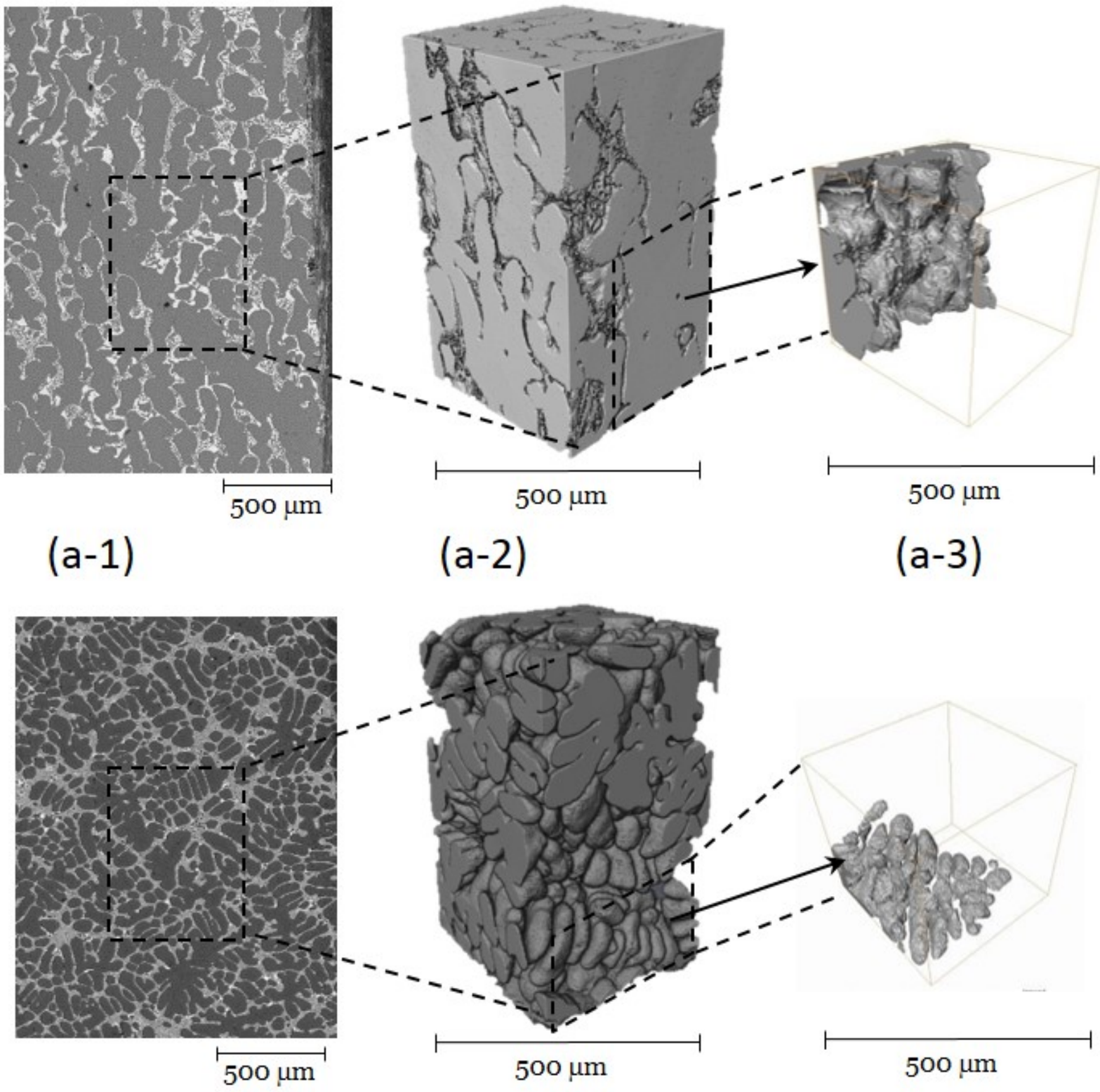

Fig. 5. The scanning electron microscopy micrographs (the images on the left), and the 3D microstructure of the Al-15%Cu cast (a) without, (b) with EMP treatment; and those for the Al-35%Cu cast (c) without, (d) with EMP.